A Lagrangian-Eulerian framework for simulation of transient viscoelastic fluid flow

Citation for the original published paper (version of record):
Ingelsten, S., Mark, A., Edelvik, F. (2019)
A Lagrangian-Eulerian framework for simulation of transient viscoelastic fluid flow
Journal of Non-Newtonian Fluid Mechanics, 266: 20-32
http://dx.doi.org/10.1016/j.jnnfm.2019.02.005

Journal of Non-Newtonian Fluid Mechanics 266 (2019) 20–32

Contents lists available at ScienceDirect

Journal of Non-Newtonian Fluid Mechanics

journal homepage: www.elsevier.com/locate/jnnfm

A Lagrangian-Eulerian framework for simulation of transient viscoelastic fluid flow

Simon Ingelsten[a,b,*], Andreas Mark[a], Fredrik Edelvik[a]

[a] Fraunhofer-Chalmers Centre, Chalmers Science Park, Gothenburg SE-412 88, Sweden
[b] Division of Engineering Materials, Department of Industrial and Materials Science, Chalmers University of Technology, Gothenburg SE-412 96, Sweden

ARTICLE INFO

Keywords:
Non-Newtonian flow
Rheology
Computational fluid dynamics
Immersed boundary methods
Confined cylinder

ABSTRACT

A novel framework for simulation of transient viscoelastic fluid flow is proposed. The viscoelastic stresses are calculated at Lagrangian nodes which are distributed in the computational domain and convected by the fluid. The coupling between the constitutive equation and the fluid momentum equations is established through robust interpolation with radial basis functions.

The framework is implemented in a finite volume based flow solver that combines an octree background grid with immersed boundary techniques. Since the distribution of the Lagrangian node set is performed entirely based on spatial information from the fluid solver, the ability to simulate flows in complex geometries is therefore as general as for the fluid solver itself.

In the Lagrangian formulation the discretization of the convective terms in the constitutive equations is avoided. No re-formulation of the constitutive equation is required for stable solutions. Numerical experiments are performed of UCM and Oldroyd-B fluids in a channel flow and of a four mode PTT fluid in a confined cylinder flow. The computed flow quantities consistently converge and agree excellently with analytical and numerical data for fully developed and transient flow.

1. Introduction

Viscoelastic flows are present in many industrial processes where it is often important to predict the outcome in terms of quality and repeatability. Simulation tools can therefore be extremely useful, but require models which accurately describe the underlying physics and that are efficiently implemented in a numerical framework.

Viscoelastic fluids are described with constitutive models that provide equations for the viscoelastic stress tensor. The Upper Convected Maxwell (UCM) model and the Oldroyd-B model [1] are generalizations of linear viscoelastic models. They do not impose any limit on polymer elongation and may therefore produce unbounded normal stresses. For the same reason they pose numerical challenges and are useful for studying the performance of numerical algorithms for viscoelastic flows [2].

Nonlinear models can describe the stresses in a more physically correct way. By adding a quadratic term to the UCM model the Giesekus model is obtained [1]. The Finitely Extensible Nonlinear Elasticity (FENE) models, e.g. FENE-P and FENE-CR [3], are derived by treating the viscoelastic fluid as a dilute solution of nonlinear, finitely extensible dumbbells. Another popular model is the PTT model, which was proposed in 1977 by Thien and Tanner [4]. The model is derived using network theory for non-affine motions between polymer chains.

Another important aspect is numerical stability. Instabilities and convergence issues can arise even for moderate Weissenberg numbers, commonly referred to as the High Weissenberg Number Problem (HWNP) [5]. Different strategies to remedy the issues have been proposed. Some aim to enhance the ellipticity of the problem through diffusion, such as Elastic-Viscous Stress Splitting (EVSS) [6] or both-sides diffusion (BSD). Other strategies are to reduce the stiffness of the equations or to preserve positive definiteness of the conformation tensor. Some examples are the Positive Definiteness Preserving Scheme (PDPS) by Stewart et al. [7], the Square Root Conformation Representation (SRCR) by Balci et al. [8], and the Log-Conformation Representation (LCR) by Fattal and Kupferman [9,10]. A comparison between different stabilization approaches can be found in Chen et al. [11].

A common approach for simulating viscoelastic flow is to solve all equations with an Eulerian discretization using finite elements [12,13] or finite volumes [14,15]. The Eulerian frame of reference is suitable for diffusion-dominated problems. Viscoelastic constitutive equations are however hyperbolic and often include no physical diffusion term. In finite volume methods, the convective term in the constitutive equation therefore needs to be discretized with specialized high-order schemes in order to avoid numerical diffusion [15].

* Corresponding author at: Fraunhofer-Chalmers Centre, Chalmers Science Park, Gothenburg SE-412 88, Sweden.
E-mail address: simon.ingelsten@fcc.chalmers.se (S. Ingelsten).

https://doi.org/10.1016/j.jnnfm.2019.02.005
Received 13 April 2018; Received in revised form 8 February 2019; Accepted 11 February 2019
Available online 12 February 2019
0377-0257/

An alternative approach is the Lagrangian frame of reference. Rasmussen and Hassager [16] developed a Lagrangian method to solve the equations of viscoelastic flow with an integral UCM model using finite elements. The entire deformation history was stored and re-meshing was necessary. Harlen et al. [17] proposed a split Lagrangian-Eulerian method in which viscoelastic Stokes flow was calculated by solving the constitutive equations in the Lagrangian frame of reference in the nodes of a co-deforming mesh. Equations for velocity and pressure were solved with an Eulerian finite element method. As the mesh was distorted the nodes were reconnected with Delaunay triangulation to form new elements. Halin et al. [18] developed a finite element method in which the constitutive equation was integrated along particle trajectories, denoted the Lagrangian Particle Method (LPM). Local polynomial approximations were fitted to the stress in each element for evaluation of the finite element integrals. At least 3 particles were therefore required in each two-dimensional element for the simulations not to fail. The method was later refined to the Adaptive Lagrangian Particle Method (ALPM) [19], in which particles were created and deleted when necessary. A fairly large number of particles was still needed for stable transient result. A backward-tracing version of the method was also later proposed, denoted BLPM [20]. Phillips and Williams [21] used a semi-Lagrangian finite volume method in which the convective terms in all equations were calculated by tracing the vertices of control volumes backwards in time. The remaining terms were then integrated over a staggered grid arrangement.

Eulerian finite volume discretization on non-staggered grids is a well-established approach in computational fluid dynamics. Additional models, e.g. coupling to heat transfer or simulation of multiphase flow with the Volume of Fluid (VOF) method can be added with the same discretization. Furthermore, the Lagrangian frame of reference may be preferable when calculating the viscoelastic stresses. Hence there is a need for a robust and efficient method to combine the two approaches.

In this paper such a framework is presented. The constitutive equation is solved at Lagrangian nodes which are convected by the fluid. The stresses are then interpolated to the fluid grid using radial basis functions (RBF) [22,23] and included in the momentum equations. The novelty of the method is in the combination of the mesh-free node set and the robust information transfer between the Lagrangian and Eulerian frames through interpolation. The method thus imposes no lower limit on the number of nodes per cell for the interpolation to succeed. In addition, the Eulerian grid never needs to be re-meshed due to distortion as in co-deforming Lagrangian approaches.

No stabilization technique other than both sides diffusion is required to obtain stable results and the framework supports viscoelastic flow in arbitrary geometry with exterior and immersed boundary conditions. The method is suitable for extension to two-fluid flows, for which the constitutive equation would only need to be solved in the viscoelastic subset of the domain.

The framework is implemented in IPS IBOFlow® [24], which is an incompressible flow solver that utilizes implicit immersed boundary methods to impose boundary conditions of interior objects in the computational domain [25,26]. The fluid momentum and continuity equations are discretized on a Cartesian octree grid which is automatically generated and dynamically refined. The solver is suitable for simulation of flows including complex moving geometries and for applications with multiple coupled physical phenomena. The solver has been successfully employed to simulate e.g. conjugated heat transfer [27], fluid-structure interaction [28] and two-phase flows of shear thinning fluids with the Volume of Fluids (VOF) method, with applications for seam sealing [29,30] and adhesive extrusion [31].

The rest of the paper is structured as follows. First the governing equations are stated, followed by a presentation of the numerical method. In the results section the accuracy and performance is validated with numerical experiments. First viscoelastic channel flow is simulated and compared to analytic solutions for steady and transient flow. The flow past a confined cylinder of a PTT fluid with four relaxation modes is then studied and the results are compared to available numerical data. Finally, the last section summarizes the paper and some future work is outlined.

2. Governing equations

Viscoelastic fluid flow is modeled with the incompressible fluid momentum and continuity equations

$$\rho\frac{\partial \mathbf{u}}{\partial t} + \rho\mathbf{u}\cdot\nabla\mathbf{u} = -\nabla p + \nabla\cdot\sigma + \mathbf{f}, \tag{1}$$

$$\nabla\cdot\mathbf{u} = 0, \tag{2}$$

where ρ is density, $\mathbf{u}$ velocity, p pressure, σ extra stress and $\mathbf{f}$ a body force. The extra stress may be decomposed in a solvent contribution and a viscoelastic contribution as

$$\sigma = 2\mu\mathbf{S} + \tau, \tag{3}$$

where μ is solvent viscosity, $\mathbf{S} = \frac{1}{2}(\nabla\mathbf{u} + (\nabla\mathbf{u})^T)$ strain rate and τ viscoelastic stress. A constitutive equation for τ can be written on the form

$$\lambda\overset{\triangledown}{\tau} + F(\tau)\tau = 2\eta\mathbf{S}, \tag{4}$$

where λ is relaxation time, F a relaxation function, η polymeric viscosity and $\overset{\triangledown}{\tau}$ the upper convected derivative of τ, reading [1]

$$\overset{\triangledown}{\tau} = \frac{d\tau}{dt} - \nabla\mathbf{u}^T\cdot\tau - \tau\cdot\nabla\mathbf{u}. \tag{5}$$

In (5) d/dt denotes the material time derivative, i.e. the Lagrangian derivative, which in the Eulerian frame of reference reads

$$\frac{d\tau}{dt} = \frac{\partial\tau}{\partial t} + \mathbf{u}\cdot\nabla\tau. \tag{6}$$

A viscoelastic material may in general be modeled with multiple relaxation modes. For a material with N modes the stress modes τ_k, where $k = 1, \ldots, N$, are then described by (4) with relaxation times λ_k, polymeric viscosities η_k and relaxation function F_k. The total viscoelastic stress is the sum of the stress modes, namely

$$\tau = \sum_{k=1}^{N}\tau_k. \tag{7}$$

3. Numerical method

A simulation framework is proposed in which the viscoelastic stresses are solved in a Lagrangian node set distributed in the viscoelastic fluid. The momentum and continuity equations (1) and (2) are solved using an Eulerian finite volume discretization and are integrated in time using the implicit Euler method. Coupling to the constitutive equation is established through the divergence of the viscoelastic stress tensor, which is interpolated to the Eulerian grid by using radial basis functions (RBF). The main steps carried out in each simulation time step are:

- Solve the constitutive equation and convect the stresses in Lagrangian nodes.
- Interpolate viscoelastic stresses to Eulerian grid using RBF.
- Integrate $\nabla\cdot\tau$ over fluid cells and add as sources in the discretized momentum equation.
- Solve the momentum and continuity equations.
- Control the distribution of Lagrangian nodes.

The involved steps are described in detail below.

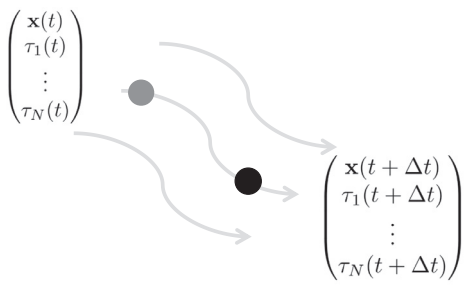

Fig. 1. Concept of Lagrangian node trajectory in the fluid flow field.

3.1. Solution of the constitutive equation

Consider a set of Lagrangian nodes distributed in the viscoelastic fluid. The position $\mathbf{x}$ of a node that is convected by the fluid is described by

$$\frac{d\mathbf{x}}{dt} = \mathbf{u}, \tag{8}$$

where $\mathbf{u}$ is the local velocity. Convection and evolution of N viscoelastic stress modes in the node are thus described by the system of ordinary differential equations (ode)

$$\begin{cases} \dot{\mathbf{x}} = \mathbf{u} \\ \dot{\tau_1} = G_1(\tau_1, \nabla\mathbf{u}) \\ \quad \vdots \\ \dot{\tau_N} = G_N(\tau_N, \nabla\mathbf{u}) \end{cases}, \tag{9}$$

where $(\dot{\bullet})$ denotes time derivative. The corresponding right hand sides G_k follow directly from the constitutive equation and are evaluated at the node. The quantities $\mathbf{u}$ and $\nabla\mathbf{u}$ in the right hand side of (9), are obtained at the node from the fluid grid by bilinear or trilinear interpolation, respectively for two and three dimensions. In Fig. 1 the concept of transporting and calculating the stresses in a Lagrangian node is illustrated.

A suitable method is needed to solve the ode system (9). In the current work it is solved using a backward differentiation formula (BDF) that is available in the Sundials CVODE library [32,33]. A linear system of equations for the solution to (9) from time t_{n-1} to t_n then takes the form

$$\Delta t_n \gamma_n \dot{\mathbf{y}}_n + \sum_{i=0}^{q} \alpha_{n,i} \mathbf{y}_{n-i} = \mathbf{0}, \tag{10}$$

where the subscript n denotes a property at time t_n, $\Delta t_n = t_n - t_{n-1}$ is the local step size, γ_n and $\alpha_{n,0}, \ldots, \alpha_{n,1}$ are coefficients, $\mathbf{y}_n$ is the solution vector and q is the order of the method. In the current work $q = 2$ is chosen due to its stability properties. More specifically it is A-stable, such that for $\kappa < 0$ the method is unconditionally stable for the scalar model problem $\dot{y} = \kappa y$ [33].

The ode system (9) is solved for a global fluid time step through multiple local time steps. The number of steps is based on local error estimation in the ode solver. For more details the reader is referred to [33].

The coupling between viscoelastic stresses and fluid momentum is explicit, since the velocity field is kept fixed when calculating the stresses and vice versa. The ode system is however solved implicitly, in the sense that $\dot{\mathbf{y}}_n$ depends on $\mathbf{y}_n$ in (10). Since $\mathbf{u}$ and $\nabla\mathbf{u}$ vary along the node trajectory they are interpolated to the node in each iteration.

For all components of $\mathbf{y}$ the relative and absolute integration tolerances are set to 10^{-6}. The tolerances correspond to the relative and absolute differences of the solved variables between two subsequent iterations. The chosen tolerances were found to produce consistent results while even smaller values did not give further improvement.

3.2. Interpolation of viscoelastic stresses

Radial basis functions (RBF) are used to interpolate the viscoelastic stress from the Lagrangian nodes to the Eulerian grid. The interpolant $\hat{f}(\mathbf{x})$ of a function $f(\mathbf{x})$, whose values are known in a set of points $\{\mathbf{x}_i\}_{i=1}^{N_c}$, is calculated as [22]

$$\hat{f}(\mathbf{x}) = \sum_{i=1}^{N_c} w_i \phi(\xi|\mathbf{x} - \mathbf{x}_i|) + \mathbf{v}^T \begin{bmatrix} 1 \\ \mathbf{x} \end{bmatrix}, \tag{11}$$

where $\{w_i\}_{i=1}^{N_c}$ are the interpolation weights, $\phi(r)$ the RBF, ξ a scaling parameter and $\mathbf{v}$ a vector of first order polynomial coefficients. The interpolation weights and the polynomial coefficients are obtained from solving the linear system

$$\begin{bmatrix} A & B \\ B^T & \mathbf{0} \end{bmatrix} \begin{bmatrix} \mathbf{w} \\ \mathbf{v} \end{bmatrix} = \begin{bmatrix} \mathbf{f} \\ \mathbf{0} \end{bmatrix} \tag{12}$$

where

$$A_{ij} = \phi(\xi|\mathbf{x}_i - \mathbf{x}_j|), \tag{13}$$

$$B = \begin{bmatrix} 1 & \cdots & 1 \\ \mathbf{x}_1 & \cdots & \mathbf{x}_{N_c} \end{bmatrix}^T \tag{14}$$

$$\mathbf{w} = [w_i \cdots w_{N_c}]^T, \tag{15}$$

$$\mathbf{f} = [f(\mathbf{x}_i) \cdots f(\mathbf{x}_{N_c})]^T. \tag{16}$$

Different choices of basis function are possible. In the current work one of Wendland's compactly supported RBF is used, reading [22]

$$\phi(r) = \begin{cases} (1-r)^2, & 0 \le r \le 1 \\ 0, & r > 1 \end{cases}. \tag{17}$$

This particular RBF is unconditionally positive definite, such that A is positive definite and (12) yields a unique solution [23].

The interpolation could in principle be performed using all points where f is known. However, since the computational cost for solving the dense system (12) increases rapidly with the number of points, only those within a search radius R_s are included. For this, $R_s = \sqrt{2}\Delta x/2$, where Δx is the local cell size, was chosen. When interpolating the stresses to a cell center the search radius then covers at least all nodes in that cell by construction. The scaling parameter $\xi = 10^{-3}$ was chosen, which was found suitable by testing the interpolation routine for a wide range of values. It is remarked that for non-uniform or unstructured grids, a relevant length scale, e.g. the longest cell side, could be chosen to define R_s.

An efficient method to find all nodes located within distance R_s from the point of interpolation is necessary to keep the computational cost low. For this an R-tree data structure from the Boost C++ libraries [34] is used, so that the nodes are spatially subdivided into boxes with decreasing size at each level. This allows for fast neighbor searches. Since R_s is defined in relation to the cell sizes of the Eulerian grid, an alternative approach would be to store the nodes residing in each cell and look in the nearest cells when searching for the nodes. The R-tree approach is however both efficient and general, as it puts no special demand on the structure of the fluid grid. It is therefore used in the current implementation but other suitable node search strategies are also possible.

3.3. Coupling between equations

The divergence of the viscoelastic stress tensor is integrated over the Eulerian control volumes and added as a source in the discretized momentum equation. In Fig. 2 a two-dimensional control volume with its faces and neighbors is shown.

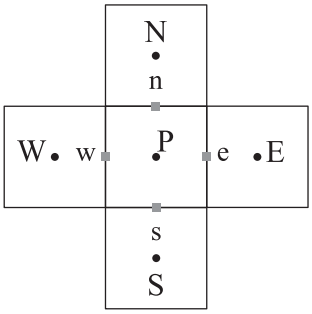

Fig. 2. Two-dimensional control volume with faces and neighbors.

The integral of the stress divergence is calculated using Gauss's divergence theorem as

$$\int_{\Delta V} \nabla \cdot \tau dV = \sum_f A_f \hat{\mathbf{n}}_f \cdot \tau_f, \tag{18}$$

where the sum is taken over the cell faces, A_f, $\hat{\mathbf{n}}_f$ and τ_f are the surface area, surface normal and viscoelastic stress, at face f, respectively. The face stress is approximated with linear interpolation from the cells sharing the face.

At wall boundaries the stresses are linearly extrapolated to the face from the value at the center of the boundary cell and its neighbor in the opposite direction from the boundary. This gives a better approximation at the face than setting the wall stress equal to the cell center value.

For calculation of steady flows, both sides diffusion (BSD) may be introduced in (1). An artificial viscous stress $\tau_b = -\mu_b \mathbf{S}$ is then added to both sides of the equation. In the discretization this term is treated implicitly as a standard viscous term on the left hand side and calculated explicitly on the right hand side. The explicit part is calculated according to the improved BSD method proposed by Fernandes et al. [35]. The velocity gradient $\nabla \mathbf{u}$ is then first calculated in each cell using central differences. The divergence term $-\mu_b \nabla \cdot \mathbf{S}$ is then calculated as for the viscoelastic stress in (18). Since the explicit and implicit parts differ whenever transient features are present in the velocity field, numerical diffusion is introduced. This results in fictitious stress responses in time dependent flow. The approach is therefore not suitable for accurate prediction of transient flows [36]. When the flow reaches a steady state, however, the explicit and implicit parts cancel. BSD may therefore be used to stabilize simulations where the final steady flow is of interest.

3.4. Node distribution

The Lagrangian nodes are distributed in the Eulerian fluid cells as follows. Each cell is divided into n_{split}^d sub-volumes, where $n_{\text{split}} \geq 1$ is the number of sub-volumes along each spatial direction and d is the dimension of the problem. A node is then placed at the center of each sub-volume. The node distribution in a two-dimensional cell is shown in Fig. 3 for $n_{\text{split}} = 2$ and $n_{\text{split}} = 3$.

During the simulation, the node set is maintained in each time step before solving the constitutive equations. A Lagrangian node is added at the center of each sub-volume that does not contain a node in its close neighborhood. The neighborhood is defined as the box with the same center as the sub-cell and with the side $\Delta x / n_{\text{split}}(1 + \epsilon_{\text{neigh}})$, where $\epsilon_{\text{neigh}} > 0$. Stresses in added nodes are interpolated from the current node set. In this work $\epsilon_{\text{neigh}} = 0.1$ was found suitable.

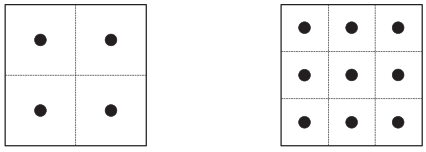

Fig. 3. Subdivision of a two-dimensional cell for distributing Lagrangian nodes with $n_{\text{split}} = 2$ (left) and $n_{\text{split}} = 3$ (right).

A number $n_{\max} \geq 1$ is also defined, corresponding to the maximum number of nodes in each sub-volume. If the number of nodes in a sub-volume exceeds $n_{\max}$, nodes are deleted until the number of nodes is equal to $n_{\max}$. This is done by identifying the pairwise closest nodes, delete them and create a new node that is given their mean position and stress. The strategy for adding and deleting nodes is inspired by that of the Adaptive Lagrangian Particle Method by Gallez et al. [19]. An addition in the current work is that also the deletion step is carried out in the individual sub-volumes.

3.5. Expected accuracy

Since the velocity gradient is required in the constitutive equation, the accuracy of the solution to the constitutive equation is limited to that of $\nabla \mathbf{u}$. For central differences, it holds that for example at cell face e

$$\left(\frac{\partial u}{\partial x}\right)_e = \frac{u_P - u_E}{\Delta x} + \mathcal{O}(\Delta x^2), \tag{19}$$

where u_P and u_E are the velocities at the current and neighbor cells sharing the face. Here (19), which can be easily be verified using Taylor expansion, is given in one dimension for simplicity. While (19) is true for the velocity gradient at the face, which is used in the discretization of the momentum equation, it is not necessarily true for arbitrary positions. Therefore the accuracy of the calculated stress can be expected to be at most second order but likely lower on average.

The accuracy of the stresses in the cell centers are further constrained by that of the interpolation routine. In simplified terms, the interpolation error depends on the distance between nodes [22]. Assume that the mean distance between two nodes is

$$l_p = \frac{\Delta x}{n_{\text{split}}}, \tag{20}$$

which is true upon initialization the node set. The interpolant can then be written as

$$\hat{f} = f + E(l_p), \tag{21}$$

where $\hat{f}$ is the interpolant, f the exact value and E denotes the error which increases with l_p.

3.6. Implementation

The proposed method is implemented in IPS IBOFlow, an incompressible Navier-Stokes flow solver. The fluid momentum and continuity equations, are discretized on a Cartesian octree grid. Boundary conditions imposed on the flow equations from internal objects are treated with the immersed boundary method [25,26]. The generation of the octree grid is fully automatic and dynamic. A key feature of the framework is therefore the capability to easily handle moving complex geometry.

One advantage with the proposed method is that discretization of the convective term in the Eulerian form is avoided. Another advantage is the geometrical flexibility resulting from the mesh-free nature of the Lagrangian node set. The only boundary condition that needs to be specified for the constitutive equation is the stress at inlets. Effects from other flow boundaries such as walls, outlets and symmetries are implicitly imposed on the constitutive equation through the velocity gradient. Thus complex geometries that can be handled by the fluid solver are also supported by the viscoelastic stress solver. Further, the mesh-free formulation avoids the need of re-meshing the Eulerian grid due to distortion, as for co-deforming mesh approaches.

Since the Lagrangian nodes in principle could be distributed in only a subset of the domain, the framework is suitable for extension to multiphase flow applications. The constitutive equation does then not need to be solved in the non-viscoelastic subset of the domain. This property

could significantly reduce the computational cost compared to using a finite volume discretization covering the whole domain. The equation system is also more or less trivially parallelizable, since the equation system for each Lagrangian node is independent of the other nodes at the time of solution.

4. Results

In this section the proposed simulation framework is validated by numerical experiments. First the method is evaluated for viscoelastic channel flow, in which the convergence towards the analytic solution is assessed. Simulations of flow past a confined cylinder of a four-mode PTT fluid are then compared to numerical results from the literature.

4.1. Fully developed channel flow

Viscoelastic flow in a two-dimensional channel is simulated and compared to analytical solutions for fully developed flow. At the inlet and outlet Dirichlet conditions are used for pressure and periodic boundary conditions are used for velocity and viscoelastic stresses. Lagrangian nodes exiting through the outlet thus re-enter at the inlet. The channel has height $2H$ and length H, where $H = 0.01$m. The choice of a relatively small length is possible due to the periodic inlet and outlet.

The flow starts at rest and a constant pressure drop is imposed over the channel through the inlet and outlet boundary conditions. Transient calculations are then carried out until the flow is fully developed. This is defined with respect to the condition

$$\frac{||\phi_n - \phi_{n-1}||}{||\phi_n||} < \varepsilon_{\text{tol}}, \tag{22}$$

where ϕ_n is velocity, shear stress or normal stress at global time step n, ε_{tol} is a tolerance, and $||\bullet||$ denotes the norm

$$||\phi_n|| = \sqrt{\sum_{i=1}^{N_{\text{cells}}} \phi_{n,i}^2}, \tag{23}$$

where $\phi_{n,i}$ is the value at the center of cell i. In all simulations of the channel flow values below $5.0 \cdot 10^{-10}$ were reached for the stresses and below $5.0 \cdot 10^{-13}$ for the velocity.

The flow is simulated for the UCM and Oldroyd-B models with a single relaxation mode. Then $F(\tau) = 1$ in (4). A viscosity ratio β is defined as

$$\beta = \frac{\mu}{\mu + \eta}, \tag{24}$$

which for the UCM model is zero by definition and for the Oldroyd-B model $0 < \beta < 1$. Here $\beta = 1/9$ is used, which is a common choice. BSD is used as stabilization due to the large stresses at fully developed conditions.

The level of elasticity is characterized Deborah number $\text{De} = \lambda U/H$ [2]. The Reynolds number is defined as $\text{Re} = \rho H U/\eta_0$, where $\eta_0 = \mu + \eta$. The parameters $\eta = 1$ Pa s and $U = 0.1$ m/s are constant and De is varied between simulations by changing λ. For all flows the $\text{Re} = 0.001$. The pressure drop over the channel corresponding to a given mean velocity is calculated from the analytic solution of Waters and King [37].

The flow is simulated with the respective models for three parameters sets. In Table 1 λ, De and the artificial viscosity μ_b are listed. The Deborah numbers cover two orders of magnitude. The values of μ_b were found suitable for stable results for the respective flows.

Table 1
Channel flow parameters.

λ (s)	De	μ_b (Pa s)
0.01	0.1	10^2
0.1	1	10^3
1	10	10^4

Table 2
Grids used in the convergence study for the channel flow.

Grid	$H/\Delta x$	#cells
G1	5	50
G2	10	200
G3	20	800
G4	40	3200
G5	80	12,800

The flows are simulated with five uniform grids of varying resolution to study the accuracy of the method. The grids are defined in Table 2. Relatively long time steps are taken, with $\Delta t/\lambda = 10^{-2}$, in order to reach fully developed flow as fast as possible.

In Fig. 4 the calculated velocity, shear stress and normal stress are shown across the channel at $x = \frac{1}{2}H$ for the UCM fluid and $\text{De} = 10$ for the grids G1, G3 and G5. The remaining two grids follow the same trends and are omitted. In these simulations $n_{\text{split}} = 2$ and $n_{\max} = 5$ are used. However, it is found that no nodes are added or deleted in this flow, so for this case the value of $n_{\max}$ is actually redundant. Velocities

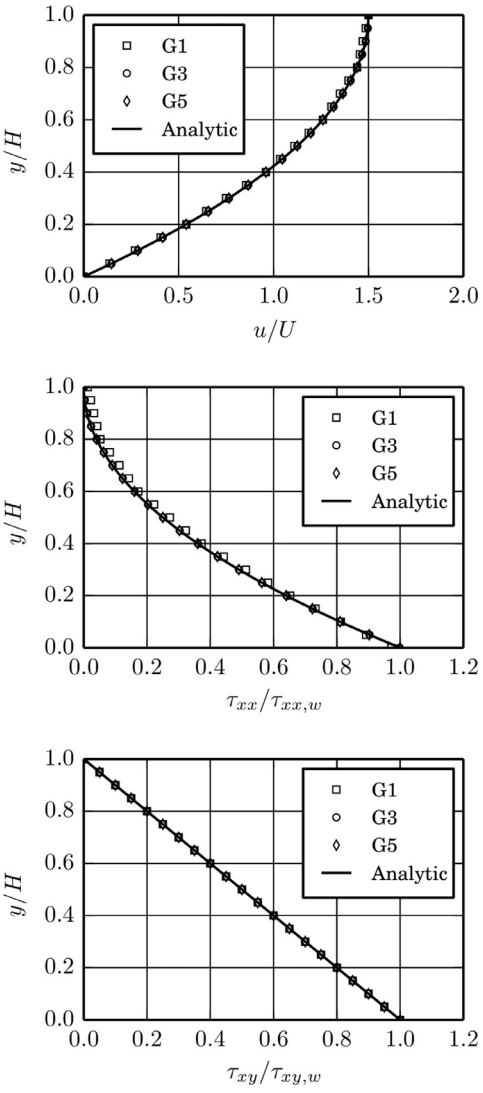

Fig. 4. Simulated fully developed velocity (top), shear stress (middle) and normal stress (bottom) calculated with the UCM model for $\text{De} = 10$. Computed using $n_{\text{split}} = 2$.

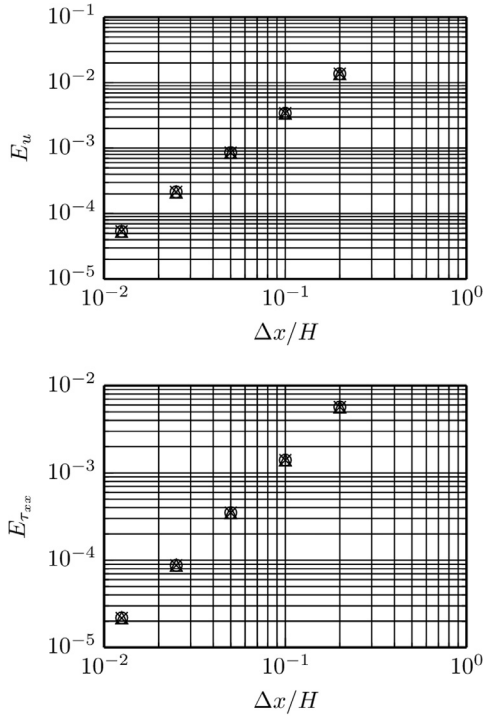

Fig. 5. Relative errors with respect to analytical solution in fully developed channel flow for velocity (top) and normal stress (bottom) for De = 0.1 (○), De = 1 (△) and De = 10 (×).

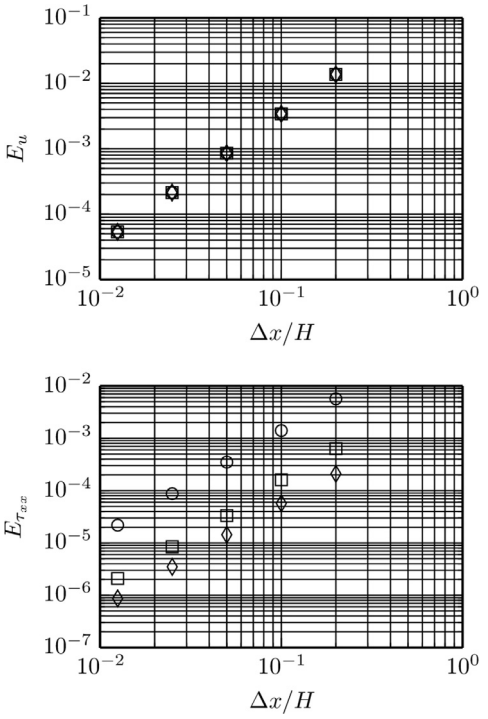

Fig. 6. Relative errors with respect to analytical solution in fully developed channel flow for velocity (top) and normal stress (bottom) for $n_{\text{split}} = 2$ (○), $n_{\text{split}} = 3$ (□) and $n_{\text{split}} = 4$ (◇).

have been normalized with U and the stresses with the analytical wall stresses $\tau_{xx,\,w}$ and $\tau_{xy,\,w}$, respectively. The velocity and normal stress clearly converge to the analytic solution with increased resolution and the shear stress practically overlaps the analytical curve for all grids.

The corresponding results for De = 1 and De = 0.1 are visually identical and are therefore omitted. The convergence rates for the three Deborah numbers are estimated using relative errors calculated as

$$E_\phi = \frac{||\phi - \phi_{\text{analytic}}||}{||\phi_{\text{analytic}}||}, \tag{25}$$

where ϕ_{analytic} is the analytic solution. Thus the errors in all computational cells contribute to the global error E_ϕ.

The relative errors of velocity and normal stress, respectively, are shown in Fig. 5. The convergence is consistent with grid refinement and practically identical for the different Deborah numbers. The order of accuracy as $\Delta x \to 0$ is estimated by the linear slope in log space for the errors obtained on the three finest grids. The resulting slopes are 2 for both the velocity and the normal stress for all three Deborah numbers. In other words the computed quantities converge with second order rate, which is the expected maximum rate due to the accuracy of the momentum and continuity discretization and of the unstructured interpolation.

Since the RBF interpolation includes a linear term and fluid discretization is second order accurate, the linear shear stress profile should in principle be calculated exactly. However, small round-off errors occur in each part of the algorithm due to the precision and tolerances of the iterative solvers. The relative shear stress errors are found to be below 10^{-9} for all simulated flows.

Another aspect of the proposed method is the resolution of the Lagrangian node set. In Fig. 6 the errors obtained on the five grids are shown for De = 0.1 using $n_{\text{split}} = 2, 3, 4$. The velocity errors overlap while the accuracy of the normal stress increases with n_{split}. The convergence with grid refinement is at second order rate for the individual values of n_{split} and is thus not affected by increased resolution of the node set. The decreased errors for increasing n_{split} instead reflect the accuracy of the unstructured stress interpolation from the nodes. Although the normal stress is more accurately predicted for larger values of n_{split}, the results suggest that increased grid resolution is the preferred refinement strategy as it also improves the accuracy of the velocity.

The simulations with the Oldroyd-B model with $\beta = 1/9$ produced results equivalent to those for the UCM model. They are therefore not subject to further discussion.

4.2. Transient channel flow

Starting from rest, a constant pressure drop is imposed over the channel and the flow is calculated over time. The Oldroyd-B model with a single relaxation mode is used and the results are compared to the analytic solution by Waters and King [37].

Again, $U = 0.1$ m/s and $\eta = 1.0$ Pa s are constant and the Deborah number is varied through λ. In addition the viscosity ratio β is varied between simulations through the solvent viscosity μ. First, flows with $\beta = 1/9, 1/18, 1/29$ are simulated for De = 0.1, 1. To avoid diffusing the solution in time $\mu_b = 0$ is used.

The computed velocity is compared to the analytical solution at the center of the channel, with equal distance to the inlet and outlet. In Fig. 7 the velocity for the first five milliseconds calculated with three time step lengths are shown for De = 0.1 and De = 1 with $\beta = 1/27$. The analytical solution of Waters and King. [37] is also included. The results are obtained with grid G3, defined in Table 2. The results clearly converge to the analytic solution and the velocities obtained with the two smallest time steps practically overlap with the analytic solution. Thus $\Delta t/\lambda = 10^{-3}$ and $\Delta t/\lambda = 10^{-4}$ for De = 0.1 and De = 1, respectively, are used for the following simulations.

The computed velocities for $\beta = 1/9, 1/18, 1/27$ are compared to the analytical solution in Fig. 8 for De = 0.1 and in Fig. 9 for De = 1. As in the temporal convergence study, the results overlap with the analytic solution in all cases.

An interesting point of study is the performance as $\beta \to 0$. The simulations are therefore repeated with $\beta = 0.001$ and $\beta = 0$ for De = 0.1. For

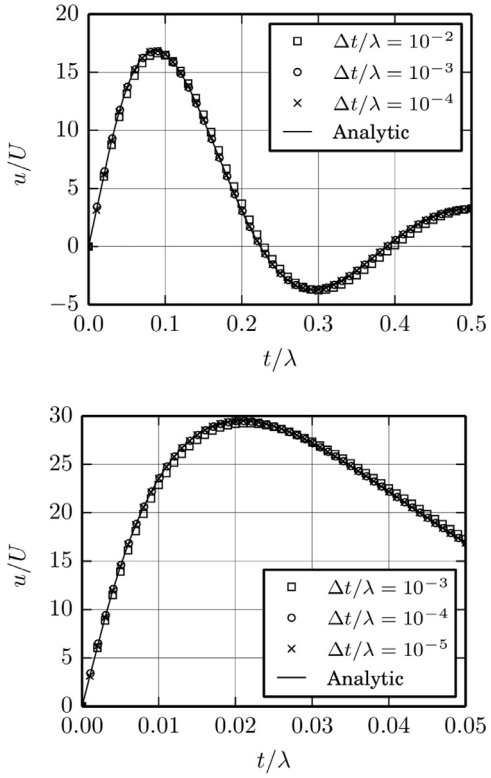

Fig. 7. Temporal convergence of centerline velocity for De = 0.1 (top) and De = 1 (bottom) with $\beta = 1/27$.

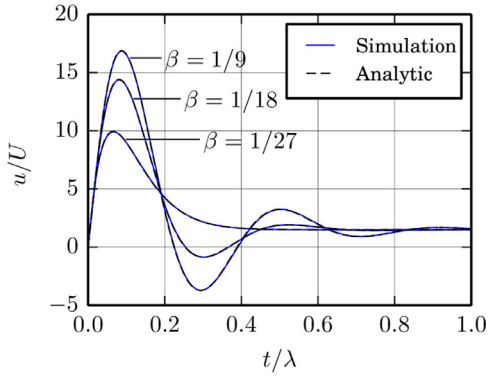

Fig. 8. Centerline velocities for transient startup of channel flow for De = 0.1.

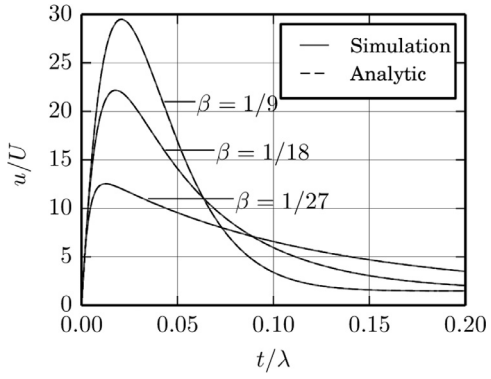

Fig. 9. Centerline velocities for transient startup of channel flow for De = 1.

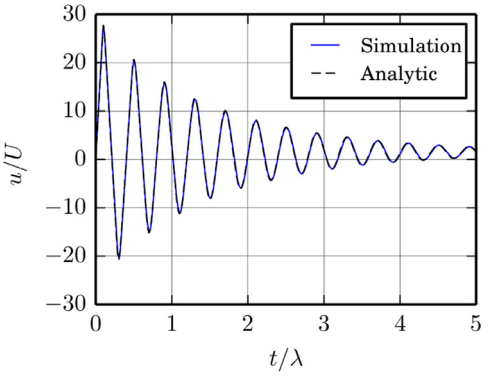

Fig. 10. Centerline velocity for transient startup of channel flow with De = 0.1 and $\beta = 0.001$.

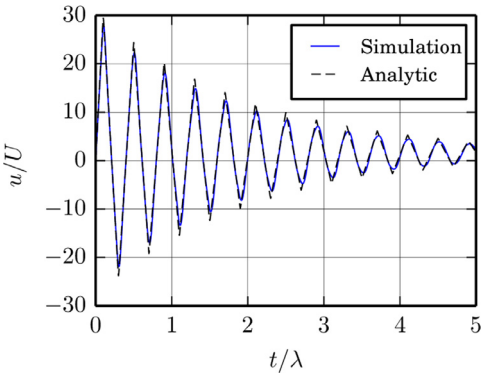

Fig. 11. Centerline velocity for transient startup of channel flow with De = 0.1 and $\beta = 0$.

these small viscosity ratios it was found necessary to introduce a small amount of BSD with $\mu_b = 0.01$ Pas to maintain the numerical stability. A smaller time step $\Delta t/\lambda = 10^{-4}$ was therefore used to reduce the effect of diffusing the solution in time. The results are shown in Fig. 10 for $\beta = 0.001$ and in Fig. 11 for $\beta = 0$. At the small yet nonzero $\beta = 0.001$ the numerical solution matches the analytic solution excellently. At $\beta = 0$, the resemblance is still good, but with some discrepancies at the velocity magnitude peaks. The frequency of the oscillations is however precisely predicted also for this case.

4.3. Confined cylinder flow

Flows past confined cylinders and spheres are commonly used as benchmark problems for viscoelastic flows, see [12–14,38,39] for some examples with models of varying complexity. Due to the confining channel and the narrowing section around the cylinder the flow includes shear and extensional characteristics, both of which are important for viscoelastic flows.

A viscoelastic polyisobutylene solution flowing past a symmetrically confined cylinder in a channel is studied. The fluid is modelled by a PTT model with four relaxation modes. The linear form of the relaxation function is used, for mode i reading

$$F_i = 1 + \frac{\varepsilon_i \lambda_i}{\eta_i} \mathrm{Tr}(\tau), \tag{26}$$

where ε_i is a non-dimensional parameter related to maximum extension of the polymer network. The values of the parameters are chosen to match those used in the FEM-simulations performed by Baaijens et al. [12] and are summarized in Table 3.

In Fig. 12 the flow geometry is illustrated. The cylinder is positioned at $x/R = 0$ and $y/R = 0$. At the inlet to the left the velocity and stress profiles obtained from simulations of 2D channel flow are prescribed.

Table 3
Parameters for the PTT model used in the confined cylinder flows.

Mode	η_p (Pa s)	λ (s)	ϵ
1	0.443	0.00430	0.39
2	0.440	0.0370	0.39
3	0.0929	0.203	0.39
4	0.00170	3.00	0.39

Table 4
Parameters for the simulations of the confined cylinder flow case.

U (m/s)	τ_0 (Pa)	De	Re
0.0115	16.9	0.25	0.019
0.0424	62.2	0.93	0.069
0.1074	157.5	2.32	0.174

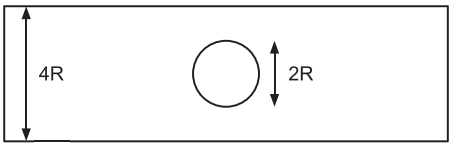

Fig. 12. Symmetrically confined cylinder geometry.

The right boundary is an outlet with zero pressure while the top and bottom boundaries are walls with the no slip condition. The total length of the channel is $20R$ with equal distance upstream and downstream of the cylinder. At the cylinder wall the implicit immersed boundary method [25,26] is used to impose the no slip condition. Stresses are extrapolated to faces inside the immersed boundary in the same way as for exterior wall faces when integrating $\nabla \cdot \tau$.

The Reynolds number is defined as $\rho UR/\eta_0$, with

$$\eta_0 = \sum_{i=1}^{4} \eta_i. \tag{27}$$

Following Baaijens et al. [12] the Deborah number, i.e. the ratio of the fluids relaxation time and the time scale of observation, is used to characterize the elasticity of the flow, defined as $\mathrm{De} = \bar{\lambda}U/R$. The mean relaxation time $\bar{\lambda}$ is calculated as

$$\bar{\lambda} = \frac{\sum_i \lambda_i \eta_i}{\sum_i \eta_i}. \tag{28}$$

Three flow rates are studied for which the parameters are summarized in Table 4. The stress value $\tau_0 = 3\eta_0 U/R$ is used to normalize the stress quantities. The elasticity number $\mathrm{El} = \mathrm{De}/\mathrm{Re} \approx 13$ for the three flows. Hence elasticity dominates inertia.

The transient flow is simulated until it is fully developed. Adaptive time steps are used, calculated such that the CFL condition $u\Delta t/\Delta x \leq 0.1$ is satisfied throughout the domain, where u and Δx are the local velocity and cell size, respectively. A small amount of both sides diffusion with $\mu_b = \eta_0$ was found sufficient for these simulations.

A grid independence study is performed for the highest Deborah number by comparing the stress and velocity profiles for the fully developed flow. Four uniform grids are used, which are defined in Table 5. For these simulations $n_{\mathrm{split}} = 2$ and $n_{\max} = 5$ are used for the Lagrangian node set. The influence of these parameters on the numerical results are discussed later in this section. The resulting adaptive time steps are approximately in the range $2.5 \cdot 10^{-4} < \Delta t/\bar{\lambda} < 1.5 \cdot 10^{-3}$ for the grids used.

Numerical results obtained with the different grids are first compared across the channel downstream of the cylinder at $x/R = 1.5$, since this is an important region of the flow. In Fig. 13 the results from the four grids are shown. Velocity is normalized by U and stress quantities by τ_0. The normal stress difference is defined as

$$N_1 = \tau_{xx} - \tau_{yy}. \tag{29}$$

Table 5
Grids used in the convergence study for the confined cylinder flow.

Grid	Δx	N_{cells}
M1	R/10	$8 \cdot 10^3$
M2	R/20	$32 \cdot 10^3$
M3	R/40	$128 \cdot 10^3$
M4	R/60	$288 \cdot 10^3$

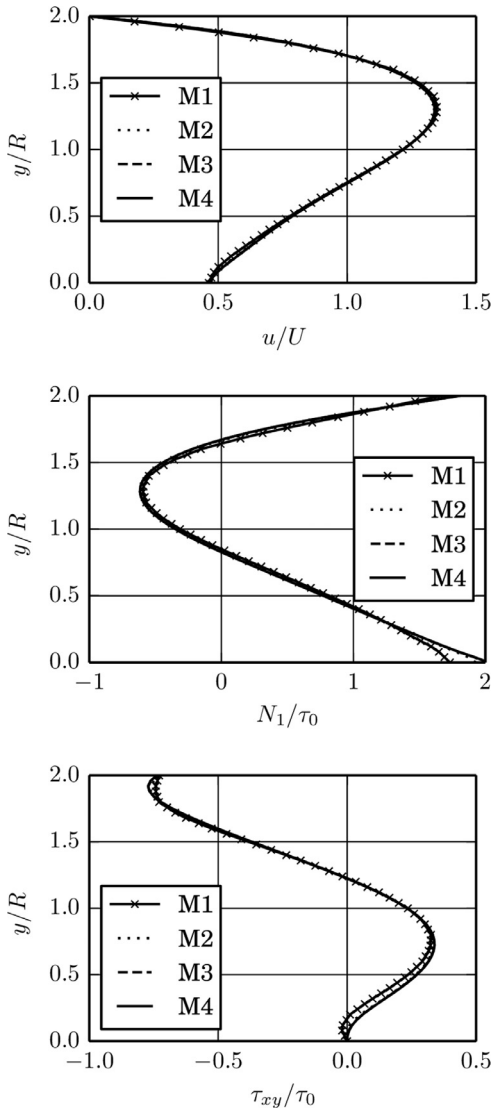

Fig. 13. Simulated U (top), N_1 (middle) and τ_{xy} (bottom) for the confined cylinder flow at $x/R = 1.5$ and with $\mathrm{De} = 2.32$ with the grids defined in Table 5.

It is obvious the resolution of the coarsest grid M1 is insufficient. The quantities calculated on the three finer grids, however, are very close across the channel. The grids are further compared by studying N_1 along the channel centerline downstream of the cylinder. The results from the different grids are shown in Fig. 14. From these results it is clear that also the resolution of grid M2 is insufficient to resolve the large variations near the stagnation point at the cylinder wall. The normal stress differences from the two finest grids, on the other hand, are very close also in this area. The remaining simulations in this section are therefore performed with grid M3.

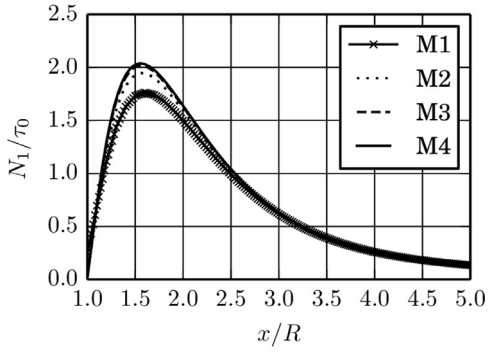

Fig. 14. Simulated N_1 for the confined cylinder flow along $y/R = 0$ and with De = 2.32 with the grids defined in Table 5.

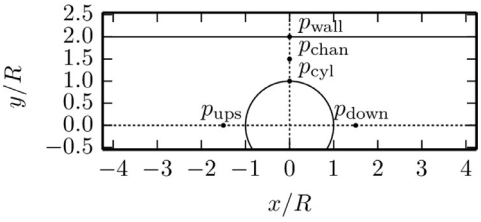

Fig. 15. Location of points in cylinder channel for monitoring transient stresses.

An important aspect of the proposed method is the behavior of the stress field near steep stress gradients, particularly how the predicted stresses are affected by how Lagrangian nodes are added and deleted between time steps. If these operations introduce significant errors to the resulting stress field, non-smooth transient variation or discontinuous jumps in the stresses would be produced. The transient stress quantities are therefore monitored in a set of relevant points.

Three points are located at the cross section $x/R = 0$, which is the narrowest part of the flow. In this area the stress gradients are large, both in the streamwise and the cross-streamwise direction, due to the combination of shear and extensional flow. Large gradients especially occur near the channel and cylinder walls. Two points along the channel centerline are also included, at $x/R = \pm 1.5$. At the upstream point, node trajectories diverge and addition of Lagrangian nodes is therefore expected. The five points are shown in Fig. 15 and defined in detail in Table 6.

The flow is simulated at De = 2.32 for $0 \le t/\bar{\lambda} \le 1/2$ using $n_{\text{split}} = 2, 3, 4$ and $n_{\max} = 3$. The amount of addition and deletion is quantified by recording the number of nodes that are added and deleted, respectively, within one cell length from each of point. In Fig. 16 the fraction of the time steps in which at least one node is added or deleted, respectively, are shown.

Node addition occurs to a certain degree near all the studied points, possibly with exception for p_{wall} where the amount is very low. The deletion follow the same trend, but is less frequent than the addition. Both operations increasingly occur as n_{split}, and thus the node density, is increased.

In Fig. 17 the obtained transient normal stress differences are shown at p_{wall}, p_{chan} and p_{cyl}, defined in Table 6. The corresponding shear

Table 6
Location of points in cylinder channel for monitoring transient stresses.

Point	x/R	y/R
p_{wall}	0	2
p_{chan}	0	1.5
p_{cyl}	0	1
p_{ups}	−1.5	0
p_{down}	1.5	0

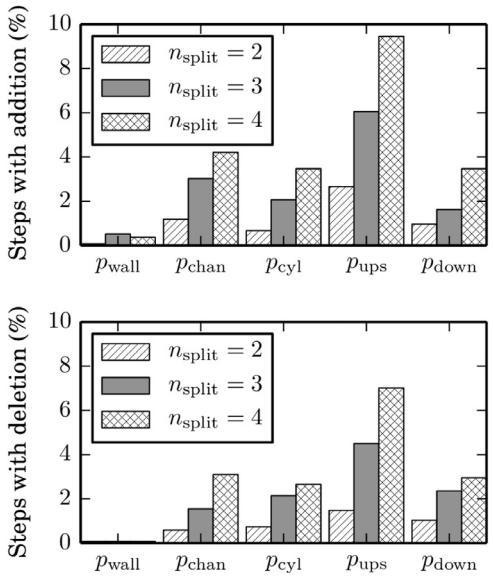

Fig. 16. Fraction of time steps with node addition (top) and deletion (bottom) for $0 \le t/\bar{\lambda} \le 1/2$ and De = 2.32 near the points defined in Table 6, using $n_{\text{split}} = 2, 3, 4$ and $n_{\max} = 3$.

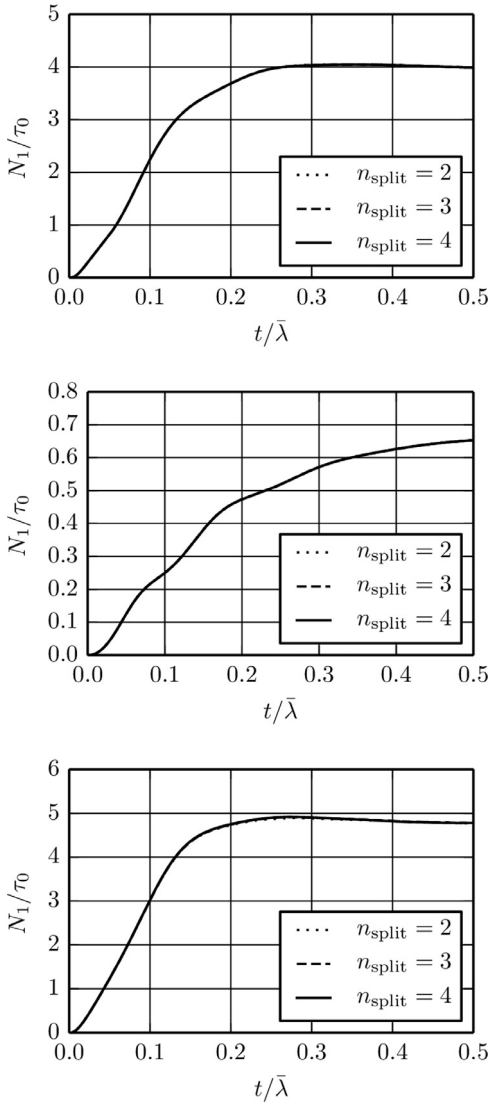

Fig. 17. Transient normal stress difference for De = 2.32 at p_{wall} (top), p_{chan} (middle) and p_{cyl} (bottom), defined in Table 6, using $n_{\text{split}} = 2, 3, 4$ and $n_{\max} = 3$.

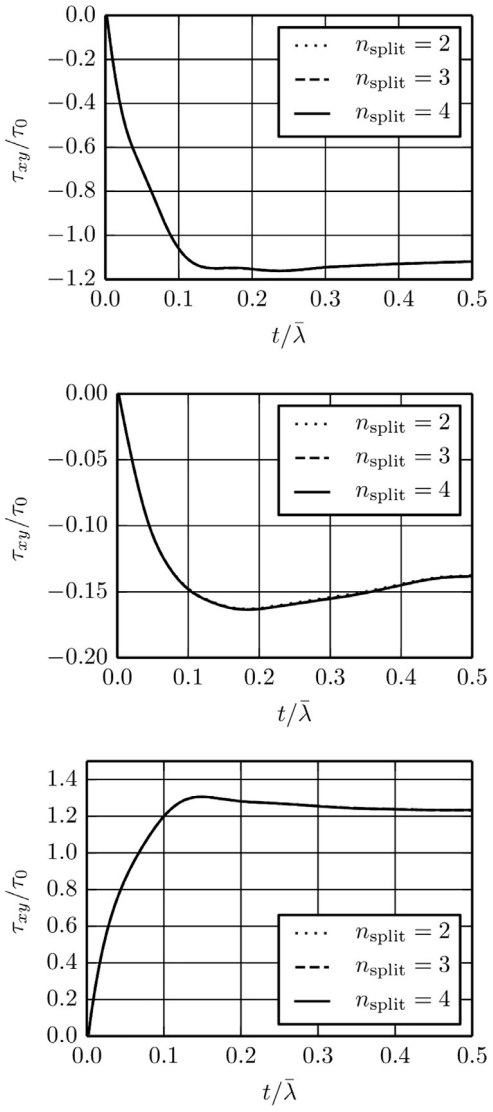

Fig. 18. Transient shear stress for De = 2.32 at p_{wall} (top), p_{chan} (middle) and p_{cyl} (bottom), defined in Table 6, using $n_{\text{split}} = 2, 3, 4$ and $n_{\text{max}} = 3$.

stresses are shown in Fig. 18. The solutions obtained with the different node sets essentially overlap, and no discontinuous jumps are observed. Similar results for p_{ups} and p_{down} are shown in Fig. 19. The shear stresses are zero along $y/R = 0$ and have therefore been omitted.

The analysis has been repeated for $n_{\text{max}} = 5$. The node addition and deletion is then less frequent, which is expected, but the transient stresses overlap those for $n_{\text{max}} = 3$. The results indicate that the errors introduced when nodes are added or deleted are very small.

It is remarked that some viscoelastic startup effects are visible in the transient curves, e.g. as smooth oscillations of N_1 at p_{chan}. The flow patterns follow from the elastic overshoot that occurs when the flow is initiated from rest, and are similar to those that were simulated for the transient channel flow, discussed in Section 4.2.

The remaining results presented have been calculated using $n_{\text{split}} = 2$ and $n_{\text{max}} = 5$, i.e. the parameters used in the grid independence study. The simulations are compared qualitatively to finite element simulations performed by Baaijens et al. [12]. This is made in cross sections and along the channel centerline $y/R = 0$. The cross sections are located in the upstream and downstream neighborhoods of the cylinder at $x/R = -1.5$ and $x/R = 1.5$, respectively, and far upstream of the cylinder at $x/R = -5$.

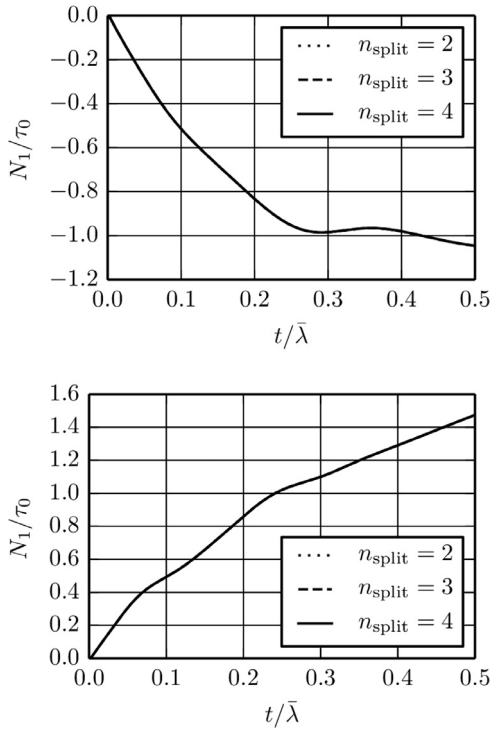

Fig. 19. Transient normal stress difference for De = 2.32 at p_{ups} (top) and p_{down} (bottom), defined in Table 6, using $n_{\text{split}} = 2, 3, 4$ and $n_{\text{max}} = 3$.

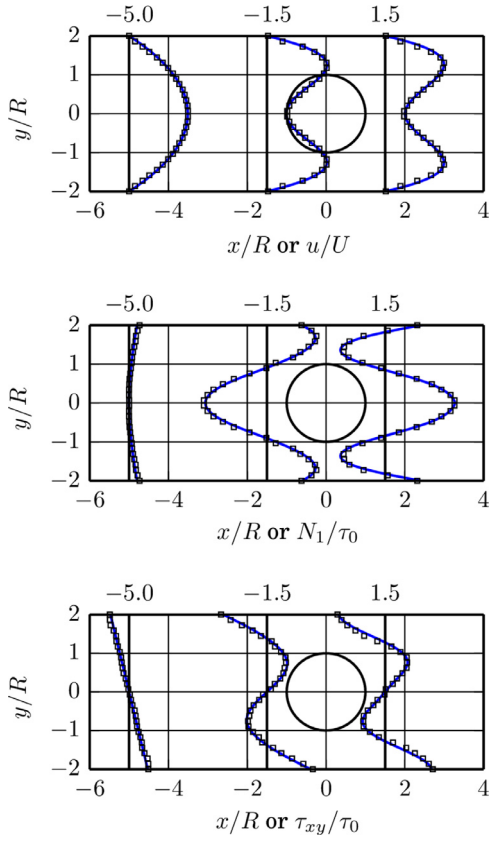

Fig. 20. Profiles of U (top), N_1 (middle) and τ_{xy} (bottom) across the channel at De = 0.25, computed with the proposed method (–) and compared to FEM-simulations (□) of Baaijens et al. [12].

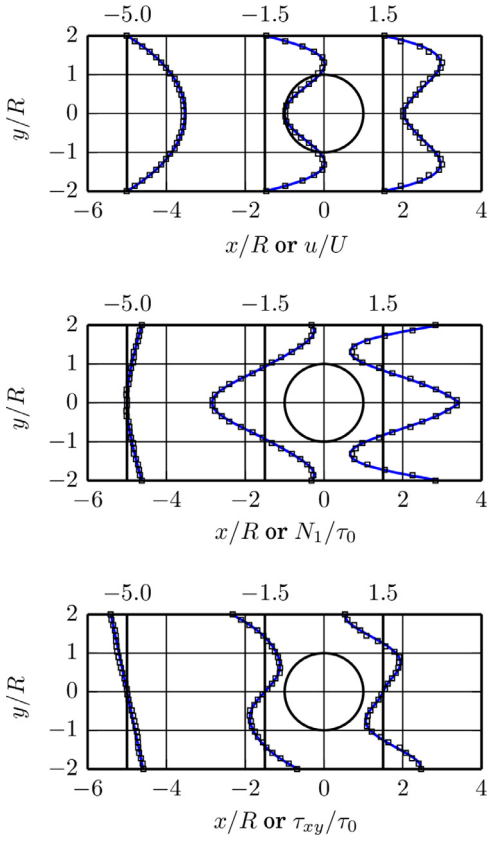

Fig. 21. Profiles of U (top), N_1 (middle) and τ_{xy} (bottom) across the channel at De = 0.93, computed with the proposed method (–) and compared to FEM-simulations (□) of Baaijens et al. [12].

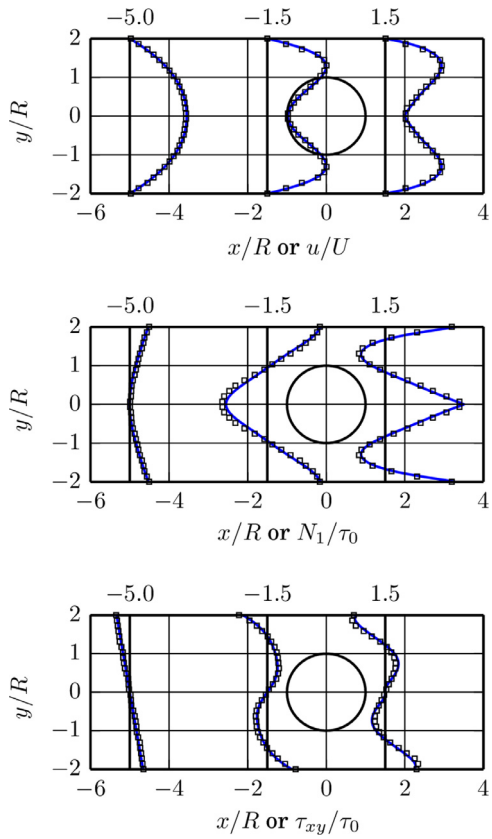

Fig. 22. Profiles of U (top), N_1 (middle) and τ_{xy} (bottom) across the channel at De = 2.32, computed with the proposed method (–) and compared to FEM-simulations (□) of Baaijens et al. [12].

In Figs. 20–22 the computed velocities and stress quantities are shown in the cross sections, respectively for the three flows. The results show overall agreement with the simulations of Baaijens et al. In particular, considering that they are produced by two completely different numerical methods. Some differences are visible at the highest Deborah number for N_1 at $x/R = -1.5$. Note however that the authors do not have access to the raw data of Baaijens et al., which could explain small discrepancies.

The results are further compared along the channel centerline, $y/R = 0$. The velocity and normal stress differences are shown in Figs. 23–25 respectively for the three flows. The shear stress is zero along $y/R = 0$ and is omitted. Again overall resemblance is found. For De = 2.32, better agreement for N_1 around $x/R = -1.5$ is observed, compared to the discrepancies in Fig. 22. Some differences in N_1 for De = 2.32 are visible downstream of the cylinder. On the contrary, the comparison across the channel in Fig. 22 suggest that the simulations are in reasonable agreement in the area.

In conclusion, reasonable agreement with the simulations performed by Baaijens et al. is obtained. Some differences are observed at the highest Deborah number. The discrepancies may however be result of uncertainties in the data.

The computational performance of the stress calculation is evaluated by simulating 100 time steps in the cylinder case with different numbers of nodes and processor threads. The results show that the simulation time is approximately proportional to the number of nodes and inversely proportional to the number of processor threads. In other words the calculation scales well with the number of nodes and is suitable for GPU parallelization. This is useful for efficient calculation of large problems.

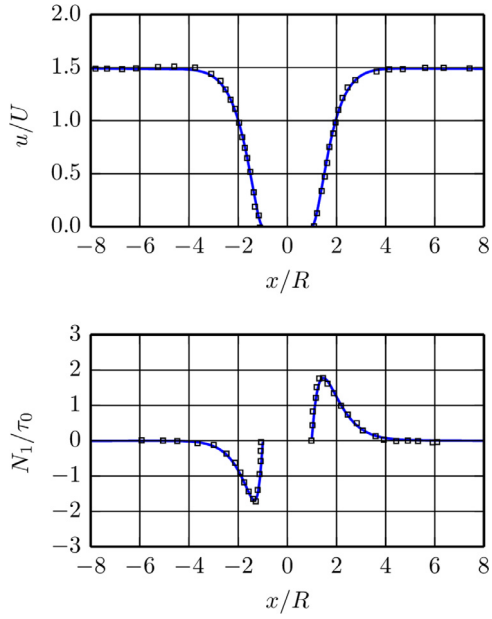

Fig. 23. U (top) and N_1 (bottom) along channel centerline at De = 0.25, computed with the proposed method (–) and compared to FEM-simulations (□) of Baaijens et al. [12].

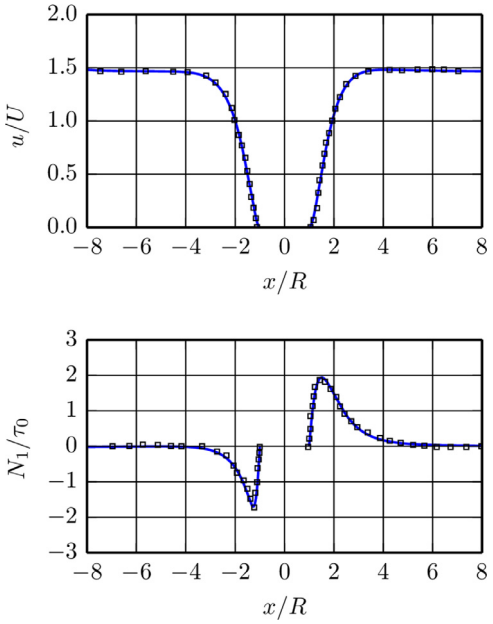

Fig. 24. U (top) and N_1 (bottom) along channel centerline at De = 0.93, computed with the proposed method (–) and compared to FEM-simulations (□) of Baaijens et al. [12].

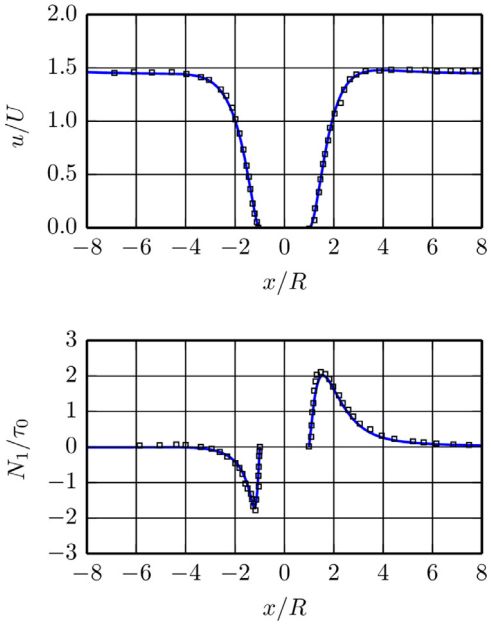

Fig. 25. U (top) and N_1 (bottom) along channel centerline at De = 2.32, computed with the proposed method (–) and compared to FEM-simulations (□) of Baaijens et al. [12].

5. Conclusion

A novel Lagrangian-Eulerian framework for simulation of viscoelastic flow has been proposed, in which the constitutive equation is solved in Lagrangian nodes that are convected by the fluid. The constitutive equation is coupled to the fluid momentum through the divergence of the viscoelastic stress. A robust and accurate radial basis function method is therefore used to interpolate the stresses to the fluid cell centers.

Numerical simulations of viscoelastic channel flow compared well with analytic solutions for fully developed and transient flows, respectively, for UCM and Oldroyd-B fluids. The simulation framework produced results with consistent convergence towards the analytic solution over a wide range of the viscoelastic flow domain.

The proposed simulation framework also produced results in good agreement with available numerical data for a more realistic viscoelastic fluid modelled as a PTT fluid with four relaxation modes in flow past a confined cylinder. This flow is of more complex nature and includes both shear flow and extensional flow characteristics. The agreement therefore further validates the simulation framework. It also demonstrates that the framework is compatible with immersed boundary methods. Further and more detailed studies of benchmark flows should however be carried out with the proposed method.

In the Lagrangian formulation of the constitutive equation, the discretization of the convective term in the corresponding Eulerian transport equation is avoided. In addition, no re-formulation of the equations, e.g. the log-conformation approach, was required to obtain stable solutions. No other stabilization than both sides diffusion was used.

The equation systems in the nodes are independent at the time of solution. The framework is therefore trivially parallelizable, which makes fast calculation of the viscoelastic stresses possible, for example through GPU acceleration. In addition, a performance study also showed that the simulations scale well with the number of nodes and the number of processor threads used for calculating the viscoelastic stresses.

The spatial discretization of the constitutive equation does not require any pre-processing step, but is reduced to the task of distributing the Lagrangian nodes throughout the fluid domain. The distribution of the node set is carried out based on information from the fluid solver where to place nodes and at which distribution density, so the flexibility and ability to simulate flow in complex geometries is as general as for the fluid solver itself. The combination of the automatically generated fluid grid and the immersed boundary method is therefore promising for simulation of viscoelastic flows in complex, possibly moving geometries. Extension to simulation of multiphase flows of viscoelastic fluids is more or less straightforward. This may be done in a computationally efficient way, as Lagrangian nodes only needs to exist in the viscoelastic part of the domain.

In conclusion, a highly capable framework for simulation of viscoelastic flows has been proposed. In future work we will present more detailed benchmark studies of the proposed method and the extension to multiphase flow in two and three dimensions, with applications in adhesive extrusion, part assembly and hemming processes.

Acknowledgments

This work has been supported in part by the Swedish Governmental Agency for Innovation Systems, VINNOVA, through the FFI Sustainable Production Technology program, and in part by the Production Area of Advance at Chalmers University of Technology. The support is gratefully acknowledged.

References

[1] R.G. Larson, Constitutive Equations for Polymer Melts and Solutions, Butterworths series in chemical engineering, Butterworth Publishers, 1988.
[2] P.J. Oliveira, F.T. Pinho, Analytical solution for fully developed channel and pipe flow of phan-thien-tanner fluids, J. Fluid Mech. 387 (1999) 271–280.
[3] M. Herrchen, H.C. Öttinger, A detailed comparison of various fene dumbbell models, J. Non-Newton. Fluid Mech. 68 (1) (1997) 17–42, doi:10.1016/S0377-0257(96)01498-X.
[4] N.P. Thien, R.I. Tanner, A new constitutive equation derived from network theory, J. Non-Newton. Fluid Mech. 2 (4) (1977) 353–365.
[5] R. Keunings, A survey of computational rheology, in: Proceedings of the XIIIth International Congress on Rheology, vol. 1, Citeseer, 2000, pp. 7–14.
[6] M. Perera, K. Walters, Long-range memory effects in flows involving abrupt changes in geometry: part i: flows associated with i-shaped and t-shaped geometries, J. Non-Newton. Fluid Mech. 2 (1) (1977) 49–81, doi:10.1016/0377-0257(77)80032-3.
[7] P.A. Stewart, N. Lay, M. Sussman, M. Ohta, An improved sharp interface method for viscoelastic and viscous two-phase flows, J. Sci. Comput. 35 (1) (2008) 43–61, doi:10.1007/s10915-007-9173-5.
[8] N. Balci, B. Thomases, M. Renardy, C.R. Doering, Symmetric factorization of the conformation tensor in viscoelastic fluid models, J. Non-Newton. Fluid Mech. 166

(11) (2011) 546–553. XVIth International Workshop on Numerical Methods for Non-Newtonian Flows. doi: 10.1016/j.jnnfm.2011.02.008.
[9] R. Fattal, R. Kupferman, Constitutive laws for the matrix-logarithm of the conformation tensor, J. Non-Newton. Fluid Mech. 123 (23) (2004) 281–285, doi:10.1016/j.jnnfm.2004.08.008.
[10] R. Fattal, R. Kupferman, Time-dependent simulation of viscoelastic flows at high weissenberg number using the log-conformation representation, J. Non-Newton. Fluid Mech. 126 (1) (2005) 23–37, doi:10.1016/j.jnnfm.2004.12.003.
[11] X. Chen, H. Marschall, M. Schäfer, D. Bothe, A comparison of stabilisation approaches for finite-volume simulation of viscoelastic fluid flow, Int. J. Comput. Fluid Mech. 27 (6–7) (2013) 229–250, doi:10.1080/10618562.2013.829916.
[12] H.P. Baaijens, G.W. Peters, F.P. Baaijens, H.E. Meijer, Viscoelastic flow past a confined cylinder of a polyisobutylene solution, J. Rheol. 39 (6) (1995) 1243–1277.
[13] M.A. Hulsen, R. Fattal, R. Kupferman, Flow of viscoelastic fluids past a cylinder at high weissenberg number: stabilized simulations using matrix logarithms, J. Non-Newton. Fluid Mech. 127 (1) (2005) 27–39, doi:10.1016/j.jnnfm.2005.01.002.
[14] P. Oliveira, F. Pinho, G. Pinto, Numerical simulation of non-linear elastic flows with a general collocated finite-volume method, J. Non-Newton. Fluid Mech. 79 (1) (1998) 1–43, doi:10.1016/S0377-0257(98)00082-2.
[15] M.A. Alves, P.J. Oliveira, F.T. Pinho, Benchmark solutions for the flow of oldroyd-b and ptt fluids in planar contractions, J. Non-Newton. Fluid Mech. 110 (1) (2003) 45–75, doi:10.1016/S0377-0257(02)00191-X.
[16] H. Rasmussen, O. Hassager, Simulation of transient viscoelastic flow with second order time integration, J. Non-Newton. Fluid Mech. 56 (1) (1995) 65–84, doi:10.1016/0377-0257(94)01274-L.
[17] O. Harlen, J. Rallison, P. Szabo, A split Lagrangian-Eulerian method for simulating transient viscoelastic flows, J. Non-Newton. Fluid Mech. 60 (1) (1995) 81–104, doi:10.1016/0377-0257(95)01381-5.
[18] P. Halin, G. Lielens, R. Keunings, V. Legat, The Lagrangian particle method for macroscopic and micro-macro viscoelastic flow computations, Dedicated to professor Marcel J. Crochet on the occasion of his 60th birthday J. Non-Newton. Fluid Mech. 79 (2) (1998) 387–403, doi:10.1016/S0377-0257(98)00123-2.
[19] X. Gallez, P. Halin, G. Lielens, R. Keunings, V. Legat, The adaptive Lagrangian particle method for macroscopic and micromacro computations of time-dependent viscoelastic flows, Comput. Methods Appl. Mech. Eng. 180 (3) (1999) 345–364, doi:10.1016/S0045-7825(99)00173-5.
[20] P. Wapperom, R. Keunings, V. Legat, The backward-tracking Lagrangian particle method for transient viscoelastic flows, J. Non-Newton. Fluid Mech. 91 (2) (2000) 273–295, doi:10.1016/S0377-0257(99)00095-6.
[21] T. Phillips, A. Williams, Viscoelastic flow through a planar contraction using a semi-Lagrangian finite volume method, J. Non-Newton. Fluid Mech. 87 (2) (1999) 215–246, doi:10.1016/S0377-0257(99)00065-8.
[22] A. Iske, Multiresolution Methods in Scattered Data Modelling, Lecture Notes in Computational Science and Engineering, vol. 37, 1ed, Springer, 2004.
[23] M.D. Buhmann, Radial basis functions, Acta Numerica 9 (2000) 138.
[24] IPS IBOFlow, http://ipsiboflow.com.
[25] A. Mark, B.G.M. van Wachem, Derivation and validation of a novel implicit second-order accurate immersed boundary method, J. Comput. Phys. 227 (2008) 6660–6680.
[26] A. Mark, R. Rundqvist, F. Edelvik, Comparison between different immersed boundary conditions for simulation of complex fluid flows, Fluid Dyn. Mater. Process. 7 (3) (2011) 241–258.
[27] A. Mark, E. Svenning, F. Edelvik, An immersed boundary method for simulation of flow with heat transfer, Int. J. Heat Mass Transf. 56 (12) (2013) 424–435, doi:10.1016/j.ijheatmasstransfer.2012.09.010.
[28] E. Svenning, A. Mark, F. Edelvik, Simulation of a highly elastic structure interacting with a two-phase flow, J. Math. Ind. 4 (1) (2014) 7, doi:10.1186/2190-5983-4-7.
[29] A. Mark, R. Bohlin, D. Segerdahl, F. Edelvik, J.S. Carlson, Optimisation of robotised sealing stations in paint shops by process simulation and automatic path planning, Int. J. Manuf. Res. 9 (1) (2014) 4–26.
[30] F. Edelvik, A. Mark, T. Johnson, J. Carlson, Math-based algorithms and software for virtual product realization implemented in automotive paint shops, in: L. Ghezzi, D. Hömberg, C. Landry (Eds.), Math for the Digital Factory, Springer-Verlag, Berlin, 2017, pp. 231–251.
[31] M. Svensson, A. Mark, F. Edelvik, J. Kressin, R. Bohlin, D. Segerdahl, J.S. Carlson, P.-J. Wahlborg, M. Sundbäck, Process simulation and automatic path planning of adhesive joining, Procedia CIRP 44 (2016) 298–303. 6th CIRP Conference on Assembly Technologies and Systems (CATS). doi: 10.1016/j.procir.2016.02.113.
[32] Suite of nonlinear and differential/algebraic equation solvers cvode, http://computation.llnl.gov/projects/sundials/cvode.
[33] A.C. Hindmarsh, R. Serban, D.R. Reynolds, User Documentation for cvode v3.1.0 (sundials v3.1.0), Sundials.
[34] Boost C++ Libraries, http://www.boost.org/.
[35] C. Fernandes, M. Araujo, L. Ferrs, J.M. Nbrega, Improved both sides diffusion (iBSD): a new and straightforward stabilization approach for viscoelastic fluid flows, J. Non-Newton. Fluid Mech. 249 (2017) 63–78, doi:10.1016/j.jnnfm.2017.09.008.
[36] S.-C. Xue, R. Tanner, N. Phan-Thien, Numerical modelling of transient viscoelastic flows, J Non-Newton Fluid Mech 123 (1) (2004) 33–58, doi:10.1016/j.jnnfm.2004.06.009.
[37] N.D. Waters, M.J. King, Unsteady flow of an elastico-viscous liquid, Rheol. Acta 9 (3) (1970) 345–355, doi:10.1007/BF01975401.
[38] M. Alves, F. Pinho, P. Oliveira, The flow of viscoelastic fluids past a cylinder: finite-volume high-resolution methods, J Non-Newton Fluid Mech 97 (2) (2001) 207–232, doi:10.1016/S0377-0257(00)00198-1.
[39] D. Fraggedakis, Y. Dimakopoulos, J. Tsamopoulos, Yielding the yield-stress analysis: a study focused on the effects of elasticity on the settling of a single spherical particle in simple yield-stress fluids, Soft Matter 12 (2016) 5378–5401, doi:10.1039/C6SM00480F.